Observations of Steady Longshore Currents in the Surf Zone

R. T. GUZA

Scripps Institution of Oceanography, La Jolla, CA 92093

E. B. THORNTON

Naval Postgraduate School, Monterey, CA 93940

N. CHRISTENSEN, JR.

Scripps Institution of Oceanography, La Jolla, CA 92093

(Manuscript received 24 February 1986, in final form 9 June 1986)

ABSTRACT

Steady surf-zone longshore currents and directional properties of the incident wave field were measured on a beach with nearly straight and parallel depth contours. Selected data were processed into 64 segments, each of 68.2 min. duration, irregularly spaced throughout an 18-day period. A wide variety of incident wave and longshore current conditions were observed. The radiation stress spectrum [$S_{xy}(f)$] was estimated from a slope array and two current meters located seaward of the surf zone. In many cases the total radiation stress [$S_{xy}^T = \sum S_{xy}(f)\Delta f$] contains important contributions from a wide range of frequencies. In a few instances, sea and swell approach the beach from different directional quadrants, resulting in a near zero S_{xy}^T. The strong shears and direction reversals of the longshore current that could conceivably occur in this circumstance were not observed. An EOF decomposition of the mean longshore current pattern shows that most (>90%) of the current spatial variation in the 64 runs is contained in a classical parabolic shape. The temporal expansion coefficients of the first EOF are equally highly correlated with both S_{xy}^T and a scale velocity suggested by radiation stress-based longshore current theories.

1. Introduction

It is well known that gravity waves which are non-normally incident on a beach can generate steady longshore currents in the surf zone. Modern theories (Bowen, 1969; Thornton, 1970; Longuet-Higgins, 1970) have theoretically established that the driving force for these currents is S_{xy}, the off-diagonal component of the incident wave-radiation stress tensor. For a monochromatic (frequency f), unidirectional (angular deviation from normal incidence Θ) wave train, to lowest order,

$$S_{xy}(f) = E(f)n \sin\Theta\cos\Theta \tag{1}$$

where $E = \rho g a^2/2$ is the energy and n the ratio of group to phase velocity. On plane parallel contours, $S_{xy}(f)$ is conserved during the shoaling processes. When the waves break, there is a decrease in the radiation stress associated with the reduction in wave energy. The longshore momentum balance becomes (schematically)

$$\frac{\partial S_{xy}}{\partial x} = D + E + \cdots \tag{2}$$

where the terms on the right-hand side are bed shear stress, turbulent momentum exchange, and other effects that involve the mean longshore current. The functional forms of the S_{xy} gradient, bed stress, and other terms involve a very considerable amount of empiricism. A large number of models differ from each other primarily in the detailed specifications of these terms. Some models also include higher-order effects, such as changes in the mean depth associated with wave setup, interactions between mean currents and gravity waves, and the nonlinearity of the incident wave field. The vast majority of the longshore current models are for unidirectional, monochromatic waves.

Although mathematically tractable and suitable for comparison to some laboratory experiments, these models do not contain the physics of the random wave fields that occur in nature. The seminal work of Battjes (1974) discussed the calculation of the radiation stress for a random, directionally spread wave field and derived a model for the associated surf-zone longshore currents. The most striking difference between the random and monochromatic models is the relative importance of horizontal eddy diffusivity (turbulent mixing) in the monochromatic models. In the random wave models, wave breaking is a statistical process and there is not a fixed "break point." The discontinuity in mean longshore velocity that occurs at the break

point of diffusionless monochromatic models does not occur in diffusionless random wave models. Thornton and Guza (1983, 1986) extended the Battjes (1974) model to include more realistic wave statistics, with qualitatively similar results.

The existing longshore current models, both deterministic and random, are restricted to incident wave fields that are narrow-banded in frequency and direction. The models have not been extended to broadband (either in frequency or direction) wave fields because of the difficulty of meaningfully parameterizing the breaking of such a wave field. For example, suppose a wave field incident on a beach is composed of two energetic frequency bands (f_1 and f_2) from different directional quadrants (for example, locally generated wind chop and swell from a distant storm). The total radiation stress is then composed of two terms of different sign, which will be assumed to be equal in magnitude:

$$S_{xy}^T = S_{xy}(f_1) + S_{xy}(f_2) = 0. \quad (3)$$

Existing models of the shoaling and breaking of both deterministic and random wave fields can predict the spatial evolution of the total energy, but not the spatial variation of the individual $S_{xy}(f_{1,2})$ terms in Eq. (3). If the breaking process extracts momentum at equal rates from both frequency components, there are no driving terms for longshore currents. On the other hand, differential breaking (i.e., one band loses momentum seaward of the other) would drive a longshore shear current with sign reversals. Although this hypothetical wave field is an extreme example, there are qualitatively similar (and quantitatively important) effects associated with all but the simplest incident wave fields. There are no longshore current models for directionally spread incident waves because there are no models describing the necessary details of the breaking process.

This constraint led Wu et al. (1985) and Thornton and Guza (1986) to consider a subset of the present observations. They selected runs with incident waves narrow-banded in frequency and direction for comparison to narrowband models. The present work examines the longshore currents observed with a wide variety of incident wave fields. The experiment and data processing are briefly described in section 2. Properties of the incident wave radiation-stress spectra are considered in section 3 and the associated currents are qualitatively discussed. In section 4, an empirical orthogonal eigenfunction (EOF) analysis is used to describe the spatial and temporal patterns of longshore current variability. The first EOF has a classic, parabolic spatial structure. In section 5, the temporal variability of the first EOF is shown to be correlated equally strongly with S_{xy}^T and with a scale velocity suggested by radiation stress-based longshore current theories. The total radiation stress, and not the structure of $S_{xy}(f)$, appears to be of primary importance to the magnitude of longshore currents.

2. Experiments

The data considered here were collected at Leadbetter Beach, Santa Barbara, California, from 29 January to 15 February 1980 as part of the Nearshore Sediment Transport Study (NSTS). General aspects of the Leadbetter Beach experiment are discussed in Gable (1981). One motivation for selecting this field site was that the very shallow water bottom contours are relatively straight and parallel (Fig. 1), which simplifies the dynamical description and analysis. A plan view of the location of sensors used in this study is also shown in Fig. 1. Rod and level surveys of the beach profile were obtained at least daily at several longshore locations by wading to approximately 100 m offshore. Complete bathymetric surveys composed of range lines at 50 m alongshore intervals extending from the beach to past the 10 m depth contour, encompassing a region 600 m upcoast (west) and 1500 m downcoast (east), were conducted on 22 January and 25 February. The daily beach profiles on 3 February and the 22 January offshore profile are connected to give the complete profiles

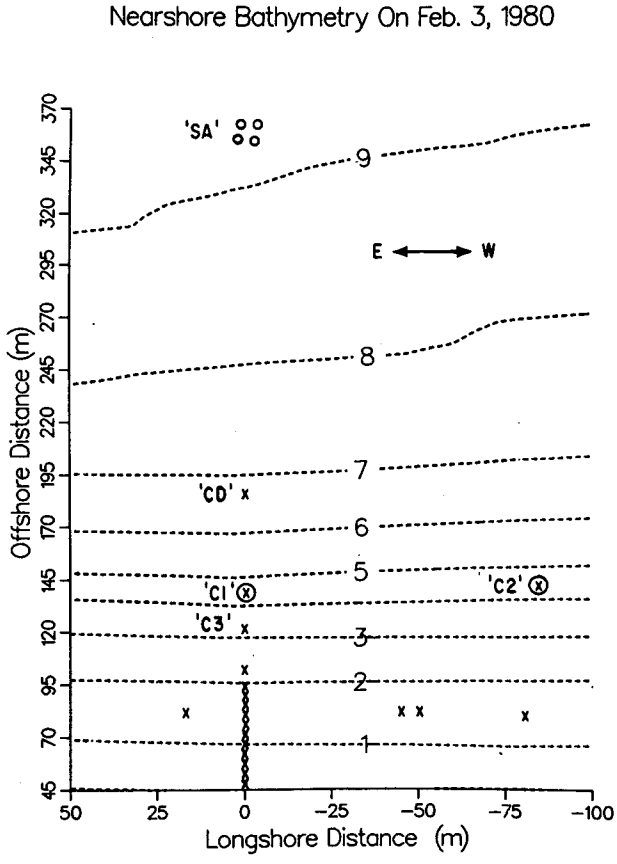

FIG. 1. Nearshore bathymetry (contours are in meters) and sensor locations on 3 February. Symbols in quotes identify sensors referred to in the text. An additional current meter at longshore location 109 m, offshore 80 m, is not shown. Electromagnetic current meters are indicated by ×'s, pressure sensors by circles.

shown in Fig. 1. Representative beach profiles are shown in Fig. 2. Data runs were at high tide with water levels between about 0 and 100 cm above MSL. Beach cusps were present in early February and had maximum amplitudes at about the 75 cm contour. The electromagnetic current meters were Marsh–McBirney model 512 with 4 cm diameter spherical probes. Based on laboratory tests, Aubrey and Trowbridge (1985) suggested that the response characteristics of these sensors may be seriously degraded in the turbulent surf-zone environment. On the other hand, Derks and Stive (1984) compared Marsh–McBirney and acoustic Vector Akwa instruments in the field and concluded that the Marsh–McBirney sensors "give the best representation of the velocity signal" at elevations greater than 20 cm above the bed. Van Heteren and Stive (1985) compared several electromagnetic and acoustic current meters in the surf zone and did not note any large discrepancies between mean flows measured by the different sensors. Calibrations provided by the manufacturer were used in the present work. Further descriptions of the sensor and their calibrations, experimental logistics and mishaps, and a discussion of the determination of the offshore direction (166.2°) are given in Thornton and Guza (1986) and references therein.

Data were acquired at a sample rate of 2 Hz for several hours each day. Sections of data subjectively judged to lack enough functioning current meters to define the cross-shore structure of the longshore current were not used. The averaging time for longshore currents was arbitrarily selected as 68.2 min., and there were 64 such runs. The minimum, maximum, and average number of functional current meters was 8, 23 and 17.5, respectively. Data from individual current meters were rejected only if the fouling, bending or other experimental malfunction was severe enough to grossly distort the mean currents compared with nearby sensors. Vector plots of the mean currents, for 17.1 minute data sections, were used for screening purposes. The longshore array of surf-zone current meters (Fig. 1) showed little longshore variation of the longshore current (for example, see Fig. 4 in Wu et al., 1985). The 64 runs were unevenly distributed throughout the 18 days spanned, although every day had at least one run. A sample of the observed 68.2 minute average longshore current patterns is given in Fig. 9 and discussed below in detail. Data from the longshore array of current meters (Fig. 1) are included in Fig. 9 and the analysis below.

3. The incident wave field

Leadbetter Beach is highly sheltered from waves generated in the open ocean because of its east–west orientation on a coastline predominantly oriented north–south. There are two directional sectors with substantial fetches (Fig. 3). The possible angular range of waves from the west window incident on the slope

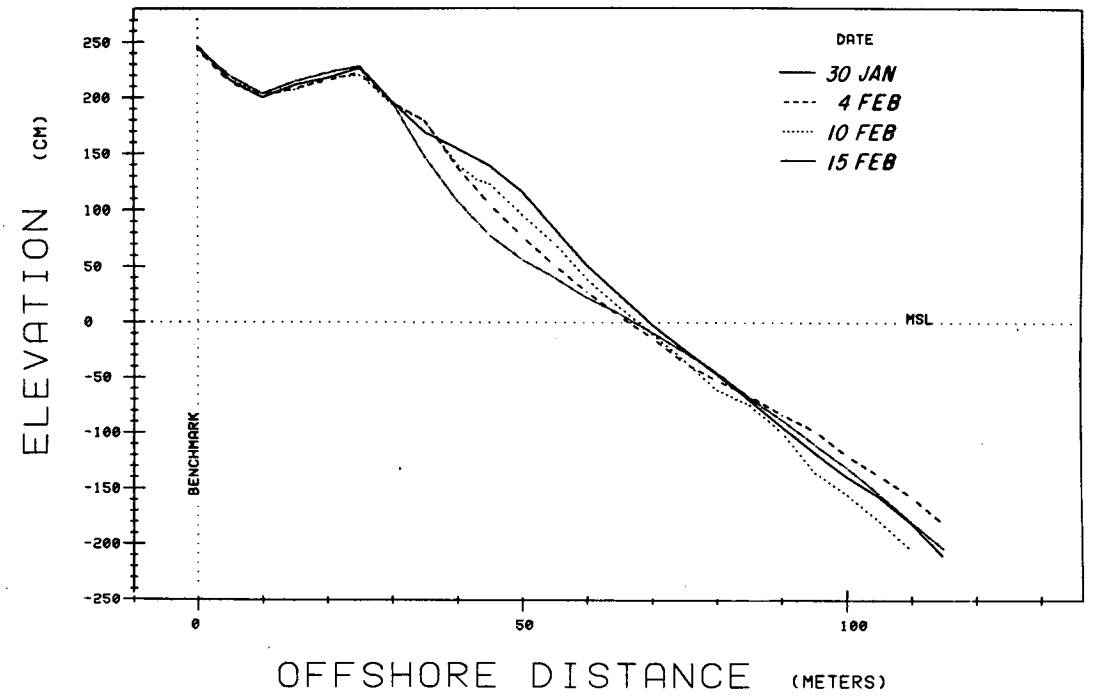

FIG. 2. Beach profiles on the instrumented transect; offshore distance is from an arbitrary datum and elevations are relative to MSL. The slope is roughly 2.5°.

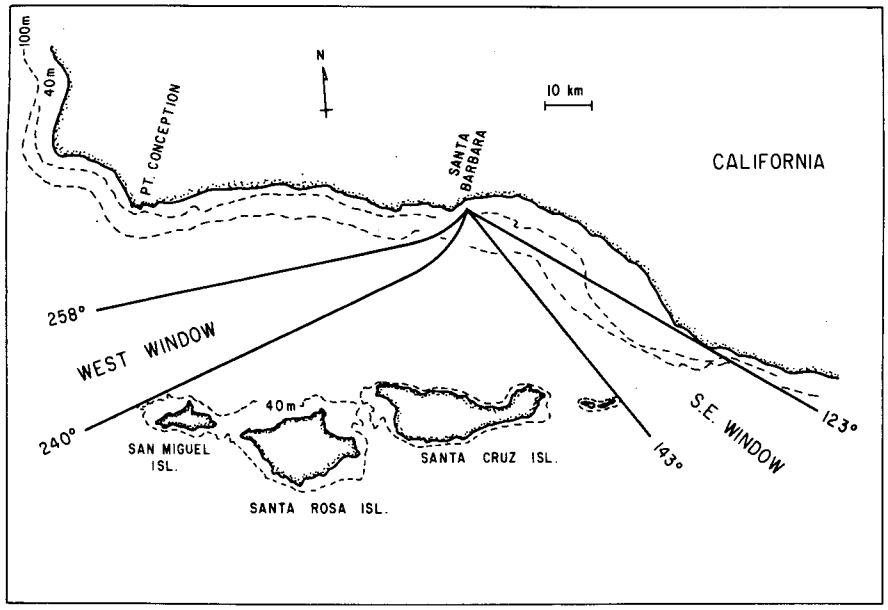

FIG. 3. Windows of significant fetch at Leadbetter Beach, Santa Barbara (Oltman-Shay and Guza, 1984).

array (SA in Fig. 1) was determined by wave refraction to be 240°–258° (Fig. 3). For example, at the predominant swell frequency of 0.075 Hz, only a small angular range of incident wave angles (at the slope array) was observed to map back into the deep ocean. Angles greater than 188° at the slope array could not escape the coastal bathymetry, while angles less than 184° hit the Channel Islands. The southeast window (123°–143° on Fig. 3) has a restricted fetch (150 km) and is not generally energetic, although substantial high-frequency energy did come from this quadrant during local storms.

Oltman-Shay and Guza (1984) used a high-resolution, data-adaptive technique to show that the directional spectra at the slope array are consistent with these topographic and refractive constraints. Wu et al. (1985) and Thornton and Guza (1986) considered five runs in which virtually all the incident wave energy was contained in a narrow (in both frequency and direction) swell peak that propagated through the west window. Details of the incident wave directional spectra are not considered in the present study.

Independent estimates of $S_{xy}(f)$ were obtained from the slope array (four pressure sensors at the corners of a 6 m square; Higgins et al., 1981) and from the two deepest current meters on the cross-shore instrument transect (CD and C1 in Fig. 1). At the slope array, $S_{xy}(f)$ was calculated from the real part of the cross-spectrum of the sea surface slope in the offshore and longshore directions (Higgins et al., 1981). The sea surface slopes were obtained by fitting a plane to the surface-corrected (according to linear theory) slope array pressure-sensor data. The value of $S_{xy}(f)$ was calculated from current meters using the real part of the cross-spectrum between onshore and longshore velocity fluctuations and applying a linear theory transfer function to integrate the cross-spectrum over depth. The total radiation stress, S_{xy}^T, is the integral of $S_{xy}(f)$ over frequency (the limits here are 0.04 and 0.4 Hz). Estimates of S_{xy}^T from the two current meters, for each of the 64 runs, are shown in Fig. 4. Wu et al. (1985) and Thornton and Guza (1986) used linear refraction to estimate the topographically induced variations in S_{xy} between the slope array and the surf zone. The five asterisks in Fig. 4 correspond to the refracted S_{xy} values and nearly coincide with the estimates from CD, but the C1 values are lower. The contours are nearly plane and parallel between CD and C1, so S_{xy} should be a conserved quantity. There does not appear to be an orientation problem with C1, because its S_{xy}^T estimates are lower than CD for waves coming from both quadrants. One plausible estimate of $S_{xy}(f)$ is the average of CD and C1. However, the S_{xy}^T estimates from C1 are nearly identical with those from CD if the energy spectrum at location 1 is estimated with a pressure sensor located there and the directional spreading estimated from C1. A second reasonable estimate of S_{xy} is the average of CD and this "corrected" C1. Fortunately, these two estimates are very similar (Fig. 5). Unless otherwise noted, all following S_{xy} values refer to the average of CD and corrected C1. In Figs. 4 and 5 and elsewhere, the ρg factors in S_{xy} [Eq. (1)] and E are not included, similar to the common convention of dropping that factor in energy spectra. The value of S_{xy}^T was also calculated with current meters C2 and C3 (Fig. 1). Although qualitatively similar to Fig. 4, the

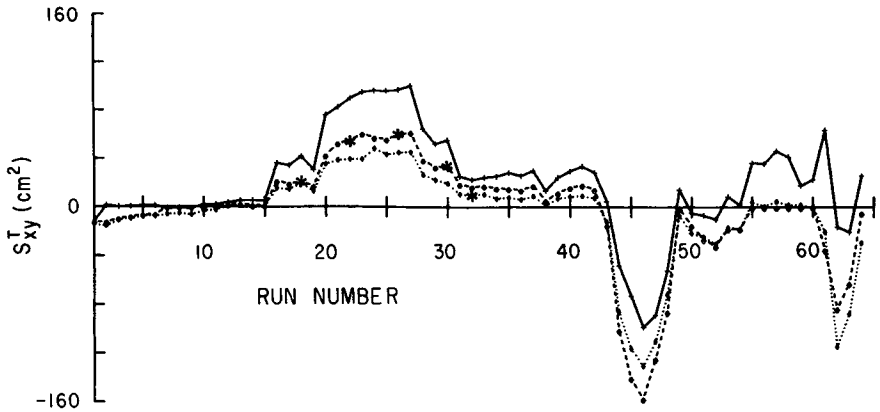

FIG. 4. Total radiation stress (S^T_{xy}) versus run number; slope array is solid line, CD dashed line, C1 dotted line, asterisks are slope-array refracted. Positive values of S_{xy} correspond to waves coming through the west window (Fig. 3).

estimates seemed noisy compared to the consistent relative values of S_{xy} from the slope array, CD and C1.

The total energy (E^T) of the sea surface elevation, averaged using CD and the pressure sensor at C1, is also shown in Fig. 5. Comparison of E^T and S^T_{xy} (Fig. 5) shows that the most energetic waves (run 62) do not correspond to the maximum S^T_{xy} (run 46). This is due to substantial amounts of energy coming from both windows (which are in different quadrants, Fig. 3) in run 62. Figure 6 compares the radiation stress spectra for runs 46 and 62. It is difficult to surmise what single values of Θ would be estimated by an observer (the

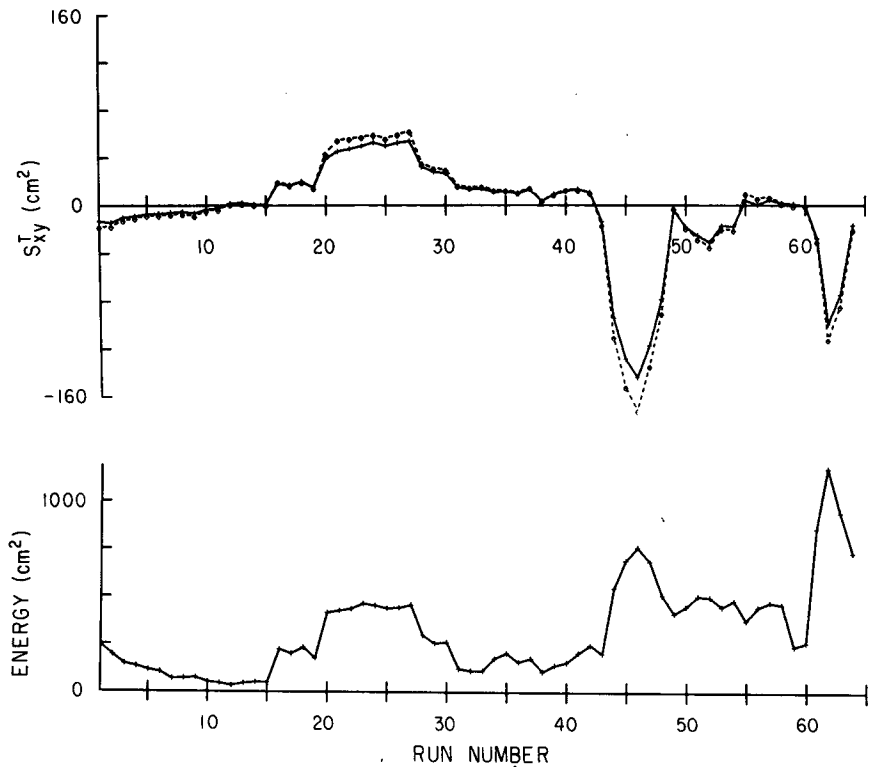

FIG. 5. S^T_{xy} versus run number; solid line is average CD and C1, dashed line is average CD and corrected (see text) C1. Lower panel is total energy ($0.04 < f < 0.4$ Hz) of sea surface elevation versus run number.

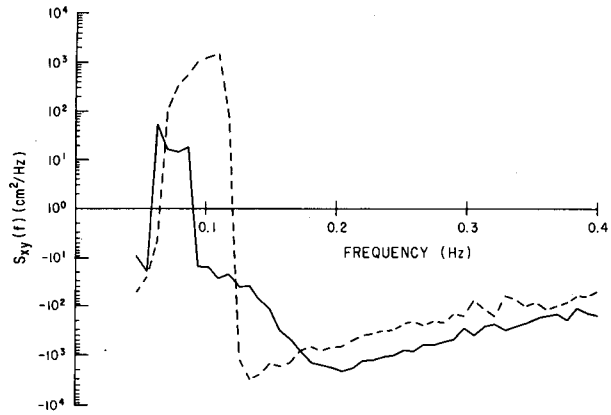

FIG. 6. $S_{xy}(f)$ spectra for the runs with maximum energy (run 62, dashed line, $E^T = 1176$ cm^2, $S_{xy}^T = -112$ cm^2) and maximum S_{xy}^T (run 46, solid line, $E^T = 759$ cm^2, $S_{xy}^T = -171$ cm^2). High frequency seas approach from the east (negative S_{xy}) and low frequency swells from the west.

method used in many longshore current studies) for run 62.

A measure of the relative amounts of $S_{xy}(f)$ coming from opposing quadrants is given by

$$r = \frac{|\sum_f S_{xy}(f)|}{\sum_f |S_{xy}(f)|} \tag{4}$$

which is plotted in Fig. 7. The values of r range from nearly unity (all waves in one quadrant) to zero (equal radiation stress in opposite quadrants). Figure 8 shows three cases of small S_{xy}^T, but widely varying r. Run 8 has only 15% of the energy of runs 56 and 58, yet has a larger S_{xy}^T. In runs 56 and 58, S_{xy}^T is the small difference of large numbers, emphasizing that S_{xy}^T is a function of both the total energy and the directional distribution of that energy.

The observed longshore currents ($\bar{V}$) for each of the runs in Figs. 6 and 8 are shown in Fig. 9 (note scale variation in plots). The largest S_{xy}^T has the strongest currents (run 46). Run 25 is associated with a very narrow-banded $S_{xy}(f)$ and energy spectra ($r = 0.996$) but has a $\bar{V}$ pattern similar (but opposite in sign) to the biquadrant run 62 ($r = 0.59$). Runs 8, 56 and 58 have comparable (weak) mean currents, consistent with

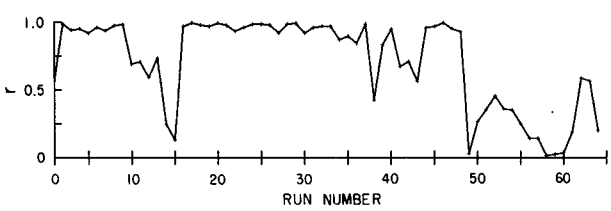

FIG. 7. A measure of the relative amount of S_{xy} in opposing quadrants [r, Eq. (4)] versus run number.

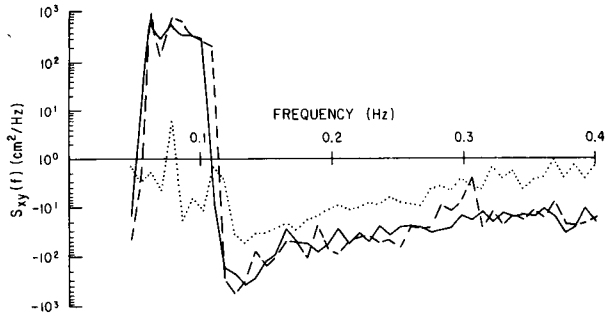

FIG. 8. $S_{xy}(f)$ for runs 8 (dotted line, $r = 0.97$, $E^T = 71$ cm^2, $S_{xy}^T = -7$ cm^2), 56 (dashed line, $r = 0.13$, $E^T = 445$ cm^2, $S_{xy}^T = 6$ cm^2) and 58 (solid line, $r = 0.04$, $E^T = 460$ cm^2, $S_{xy}^T = 1.6$ cm^2).

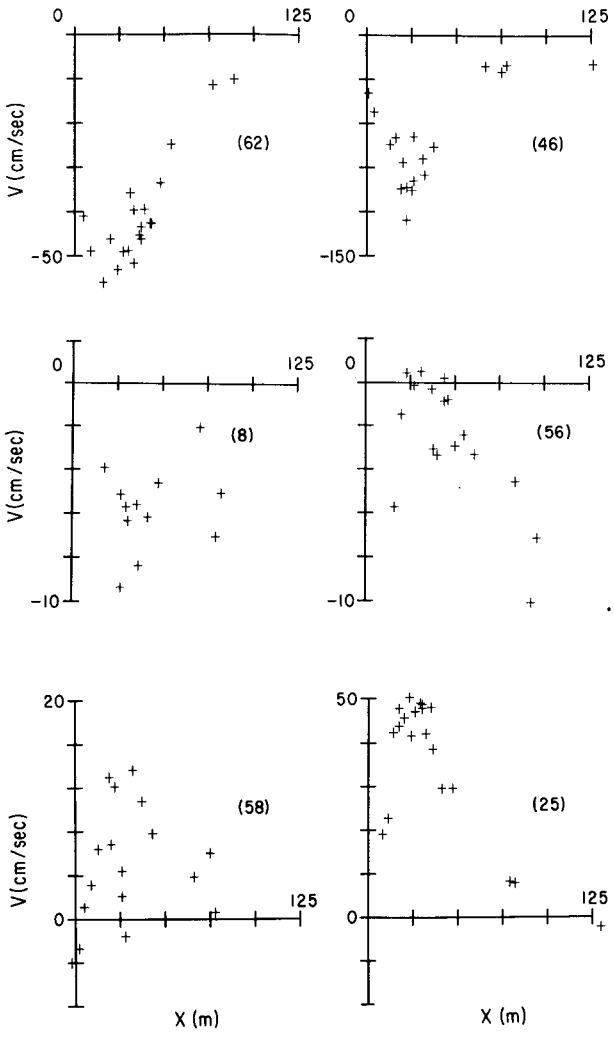

FIG. 9. Longshore current ($\bar{V}$) versus offshore distance (x) from the still water line. Run numbers are indicated in parentheses on each panel. Note that the velocity scale changes from panel to panel. Positive currents flow from west to east, as would be expected with positive S_{xy}.

the small S_{xy}^T values. Apparently the strong bidirectionality of runs 56 and 58 does not lead to significant current reversals, suggesting that the structure of $S_{xy}(f)$ is of secondary importance to V, compared to the importance of S_{xy}^T. Run 56 has a positive S_{xy}^T and a weak, negative, mean longshore current. Opposing currents and radiation stress occurred in a few runs (Fig. 12), all with small r values. In these cases, small errors in either sensor alignment or the definition of the beach coordinate frame is sufficient to change the sign of the measured S_{xy}^T. The observed spatial variation of strong currents is usually smoother than occurs with weak currents (runs in Fig. 9 are typical). The spatial variability of the weak currents is believed to be associated with the roughly ± 5 cm s^{-1} measured mean-flow uncertainty resulting from errors in the sensor offset at zero flow and from biases introduced by the sensor response in asymmetric reversing flows (Cunningham et al., 1979). The average (over all sensors and all runs) longshore current is -1.3 cm s^{-1}, consistent with the small average S_{xy}^T of -5.5 cm^2.

4. Spatial and temporal variation of $\bar{V}$

Empirical orthogonal eigenfunction analysis was used to obtain a compact representation of the modes of variability of $\bar{V}$. The temporal variability of $\bar{V}$ will be shown (section 5) to be highly correlated with variations in incident wave properties. Several EOF representations were constructed. In the first case, the cross-shore transect was divided into ten bins of equal width (12 m), starting at the beach and proceeding seaward. Mean currents from all sensors in a given bin, for each run, were averaged together. The ten bins covered 120 m, the approximate width of the cross-shore current meter array (Fig. 1). The resulting 640 data points (64 runs $\times$ 10 spatial bins) formed the data matrix for EOF analysis (for example, Kundu et al., 1975). The first eigenfunction contained 89% of the variance. To give better spatial resolution in shallow water where there are more sensors and greater velocity shears are anticipated, a second EOF used narrower bins near the shore (the first seven bins were 6 m wide, the next two bins were 12 m, and the last 54 m). The first eigenfunction contained 93% of the variance. The third EOF calculation was similar to the second in that spatial bins were narrowest near shore, but different in that the bin widths varied from run to run, depending on the wave height (in case 2 the shallow water bin width is constant, 6 m). That is, with x_j the seaward boundary of the jth spatial bin,

$$x_j = \begin{cases} js, & 1 \leqslant j \leqslant 7 \\ 7s + (j-7)2s, & 8 \leqslant j \leqslant 9 \\ 20s, & j = 10 \end{cases} \qquad (5)$$

with $s = 6$ m for case 2, and $s = 25\sigma$ (σ^2 = variance of offshore sea surface elevation) for case 3. Since $H_s = 4\sigma$, the bin dimensions are equal when $H_s = 96$ cm. If all the observed longshore current profiles had similar shapes and a cross-shore scale that varied linearly with H_s, then case 3 would explain more of the variance than case 2. It turned out that the first spatial mode of case 3 described 93% of the variance, the same as case 2. Numerous other schemes for scaling the offshore coordinate were tried, including separate dependences on high-, mid- and low-frequency incident wave components. In no case did the first EOF explain more than 95% of the variance. Case 3 is selected for detailed discussion because of its simplicity and because of its correspondence with the intuition that the surf zone width (and offshore extent of the longshore current) increases with increasing wave height. The spatial variation of the first EOF of case 3 is shown in Fig. 10. The cross-shore dependence is basically parabolic, although the most shoreward position has a relatively stronger velocity than classical models, which have zero velocity at the shoreline (e.g., Bowen, 1969). Figure 10 is qualitatively similar to the cross-shore dependencies observed by Putnam et al. (1949), Kraus and Sasaki (1979), Allender and Ditmars (1981), Kraus et al. (1982), and others. The maximum longshore current occurs in spatial bin 4, which is centered at an offshore distance of 87.5σ. Using $H_s = 4\sigma$ and a nominal beach slope of 0.042, the bin is centered at a depth $h_4 = 0.9H_s$. With a nominal surf zone width based on $H_s = 0.5h_b$, the maximum current occurs near the middle of the surf zone. The shape of the first EOF could be used to determine a best-fit value for the lateral mixing coefficient in longshore current models with monochromatic incident waves. This calculation is not performed here because we suspect that, when applied to field situations, the lateral mixing coefficient in monochromatic models is more a parameterization of the randomness of wave breaking than of turbulent Reynold's stresses (Thornton and Guza, 1986). The temporal

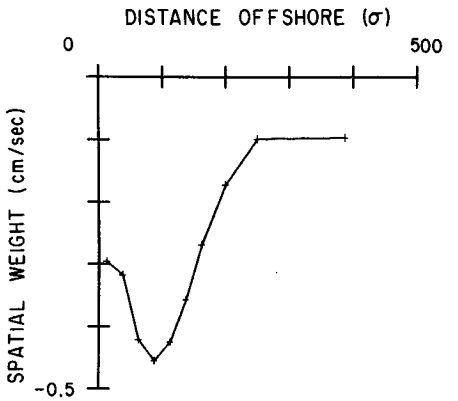

FIG. 10. Spatial weights versus offshore distance for the first EOF (93% of variance). The offshore coordinate is in units of σ, where σ^2 is the offshore sea surface variance. If $H_s = 1$ m, then $\sigma = 0.25$ m and the maximum offshore distance shown is 125 m.

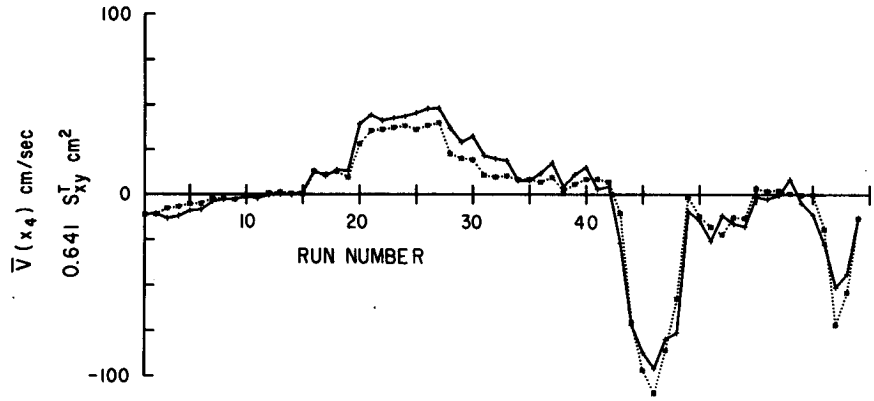

FIG. 11. Maximum longshore velocity [spatial bin 4, $\bar{V}(x_4)$, solid line] and the best linear fit total radiation stress ($0.641S^T_{xy}$, dotted line) versus run number.

variation of the magnitude of the longshore current spatial pattern is given by the temporal expansion coefficients (Fig. 11). The temporal expansion coefficient has been multiplied by the weight of spatial bin 4, so Fig. 11 shows the temporal variation of the maximum longshore current of the first EOF, $\bar{V}(x_4, t_j)$, $j = 1, 2, \cdots, 64$.

5. Incident wave–$\bar{V}$ relationships

The scatter plot of $\bar{V}(x_4, t_j)$ and $S^T_{xy}(t_j)$ (Fig. 12) shows these variables to be highly correlated (correlation = 0.97). The slope of the best-fit regression line constrained to pass through the origin is 0.641, and $0.641S^T_{xy}$ and $\bar{V}(x_4)$ are plotted in Fig. 11. Thus, the spatial and temporal variation of mean longshore currents of this dataset can be efficiently expressed as

$$\bar{V}(x_i, t_j) = BS^T_{xy}(t_j)W(x_i)/W(x_4) \tag{6}$$

where $B = 0.641$ (cm s)$^{-1}$, $W(x_i)$ are the weights of the ith spatial bin (Fig. 10), the bin boundaries depend linearly on H_s [Eq. (5)], and S^T_{xy} has units of cm^2 (no ρg factor).

Equation (6) is based on a linear regression between the temporal variation of the longshore current magnitude [$V(x_4, t_j)$ and the total applied radiation stress ($S^T_{xy}(t_j)$]. Crude scaling arguments suggest an alternative way of parameterizing the incident wave forcing and put the results in a more conventional form.

In the absence of eddy diffusivity, the surf-zone longshore momentum balance with a linearized bed-shear stress is (Longuet-Higgins, 1970)

$$\frac{\partial \hat{S}^T_{xy}}{\partial x} = \rho C_f |\tilde{u}| \bar{V} \tag{7}$$

where the caret indicates a term (in this case $\hat{S}^T_{xy}$) has the correct ρg factor, C_f is a quadratic drag law coefficient, and $\tilde{u}$ is the oscillatory component of the cross-shore velocity field. For a Rayleigh distribution of wave heights and for shallow water waves (Thornton and Guza, 1986)

$$|\tilde{u}| = (2\hat{E}/\rho\pi h)^{1/2} \tag{8}$$

where h is the depth, and the total energy $\hat{E}$ has the ρg factor. Using (8) in (7) and estimating the radiation stress gradient as $\hat{S}^T_{xy}/x_b$, with x_b a nominal break point, yields a scale velocity

$$\bar{V}^* = (\beta \hat{S}^T_{xy}/C_f)\left(\frac{\pi}{2\rho \hat{E}_b h_b}\right)^{1/2}. \tag{9}$$

For a monochromatic, unidirectional wave train, S_{xy} and E are simply related and Eq. (9) reduces (except for constant factors) to the scale velocity of Longuet-Higgins [1970, Eq. (53)]. Terms evaluated at the

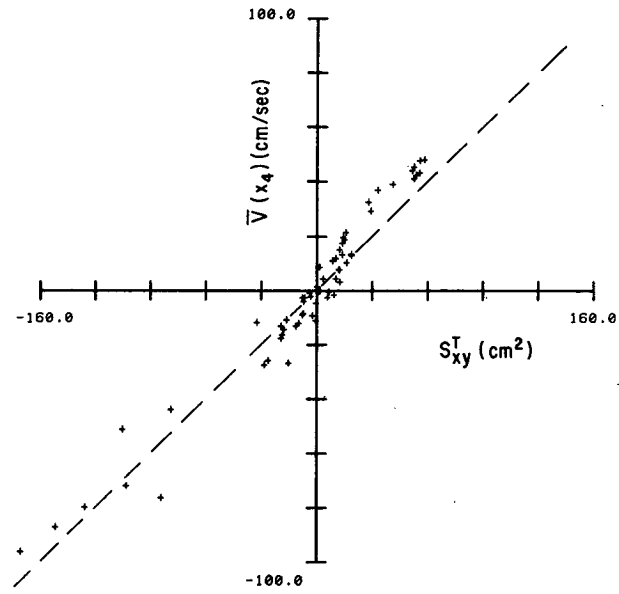

FIG. 12. Scatter plot of $\bar{V}(x_4)$ versus S^T_{xy} for all 64 runs (correlation = 0.97). The dashed line is $\bar{V}(x_4) = 0.641S^T_{xy}$.

breaker location in Eq. (9) are related to offshore (4 m depth) measurements via energy conservation

$$\hat{E}_b = (\hat{E}C_g)^T/(gh_b)^{1/2} \quad (10)$$

where it has been assumed that the waves at x_b are in shallow water, but they are not necessarily in shallow water at the offshore measurement point. Substituting Eq. (10) in Eq. (9) and letting $h_b \sim \gamma^{-1}H_{\text{rms}}$ yields

$$V^* = \left(\frac{\pi}{2\rho}\right)^{1/2}\left(\frac{g\gamma}{2\sqrt{2}}\right)^{1/4}\left(\frac{\beta}{C_f}\right)f[\hat{E}, \hat{S}_{xy}^T, (\hat{E}C_g)^T] \quad (11)$$

with

$$f = \hat{S}_{xy}^T(\hat{E}/\rho g)^{-1/8}[(\hat{E}C_g)^T]^{-1/2}$$

evaluated seaward of the breaking zone (at locations D and 1 in the present case). Although Eqs. (6) and (11) both have a linear dependence on $\hat{S}_{xy}^T$, Eq. (11) also has an $E^{-5/8}$ variation associated with the increasing surf zone width and bed shear stress occurring with increasing wave heights. Note that the use of $h_b = \gamma^{-1}H_{\text{rms}}$, where H_{rms} is measured in 4 m depth rather than in the breaker zone, is not critically important because γ appears only to the ¼ power in Eq. (11).

The quantity f [Eq. (11)] was linearly regressed against the maximum longshore current of the first EOF [$\bar{V}(x_4)$, as in Figs. 11 and 12]. No attempt was made to include variations in β/C_f between runs. Equating the slope of the regression line to the constant factors in Eq. (11) yields $C_f = 0.008$ (using average values of $\gamma = 0.43$, $\beta = 0.042$ from Thornton and Guza, 1986). This C_f value is similar to that obtained by Wu et al. (1985) and Thornton and Guza (1986) using detailed dynamical models and five runs with narrowband spectra. Exact correspondence is, of course, not expected because Eq. (11) is based on simple scaling arguments. The point is that the present observations, which include both broad- and narrowband spectra, imply C_f values, which are not radically different from directionally simpler cases. The correlation between $V(x_4)$ and f is 0.97, the same as the correlation between $\bar{V}(x_4)$ and S_{xy}^T. The introduction of relatively crude dynamical arguments [Eq. (11)] does not increase the correlation with observed currents above that with the radiation stress alone [Eq. (6)].

6. Discussion and conclusions

Qualitative comparison of $S_{xy}(f)$ and the associated longshore currents (for example, Figs. 6, 8, 9), and the high correlation between S_{xy}^T and $\bar{V}(x_j)$, suggests only a weak longshore current response to directional spectra which have small S_{xy}^T because of canceling contributions from different quadrants. This conjecture is supported by an EOF analysis using a data matrix that contains both longshore current and $S_{xy}(f)$ information. The longshore current data was distributed as in Eq. (5) (i.e., ten spatial bins and $s = 25\sigma$). The radiation stress spectra for each run was smoothed into ten frequency bands. To give the current and $S_{xy}(f)$ information equal weighting in the EOF analysis, all $S_{xy}(f)$ values were multiplied by a single constant factor. This factor was chosen so that there is equal variance in the current and $S_{xy}(f)$ data over all 64 runs [i.e., the sums of the first ten diagonal elements (currents) of the data covariance matrix is made equal to the sum of the last ten $S_{xy}(f)$]. Figure 13 shows the first (55% of total variance) and second (14%) EOFs and their temporal expansion coefficients. The weights for $S_{xy}(f)\Delta f$ (Fig. 13b) have been renormalized back into physical units. The weights for the currents in the first EOF (Fig. 13a, solid line) are nearly identical to those with only currents in the data matrix (Fig. 11). The $S_{xy}(f)$ spectra associated with the first EOF (Fig. 13b, solid line) is unimodal and has small weights relative to the currents [$\sum W^2(x_i) = 0.93$, $\sum W^2(f_i) = 0.07$, $i = 1, \cdots, 10$, with $W(x_i)$ and $W(f_i)$ the weights for current spatial bins and $S_{xy}(f)$ spectral bands, respectively]. Thus, the first EOF of a data matrix containing both currents and $S_{xy}(f)$ represents almost all the variation of the currents and only a small (but uniquadrant) part of the $S_{xy}(f)$ variation. The temporal expansion coefficient of the first EOF (Fig. 13c, solid line) is similar (except for a sign reversal of no consequence) both to the temporal expansion coefficients using currents alone and to S_{xy}^T (Fig. 11).

The second combined [$\bar{V}$ and $S_{xy}(f)$] EOF carries mostly $S_{xy}(f)$ variation [$\sum W^2(x_i) = 0.02$, $\sum W^2(f_i) = 0.98$; $i = 1, \cdots, 10$]. The $S_{xy}(f)$ spectrum is strongly biquadrant (Fig. 13b) and has nearly zero S_{xy}^T[$\sum W(f_i) = 0.71, 0.11$ for first and second EOF modes, respectively]. Thus, the second combined EOF is a mode dominated by $S_{xy}(f)$ variations with small S_{xy}^T. The associated longshore currents are very weak. The combined EOF analysis does not give any indication of a consistent pattern of significant currents associated with a biquadrant $S_{xy}(f)$.

The principal result of the present analysis is the apparent insensitivity of both the magnitude and the cross-shore variation of surf-zone longshore currents to the structure of $S_{xy}(f)$. We tentatively interpret this observation as implying that shallow-water wave breaking occurs as a broadband process extracting energy and momentum simultaneously from many incident-wave frequency bands and directions. An alternative explanation is that differential breaking does occur, but that turbulent momentum exchanges (eddy mixing) suppress strong shear currents. A detailed examination of the cross-shore variation of wind wave energy and S_{xy} spectra in the surf zone may help resolve this question, and such work is underway.

Most of the observed temporal and spatial variation of the observed longshore currents is consistent with dynamical expectations. However, the data are equally well described by alternate, even simpler approaches. For example, in the EOF analysis of currents alone (section 4), the cross-shore scale of the current pattern

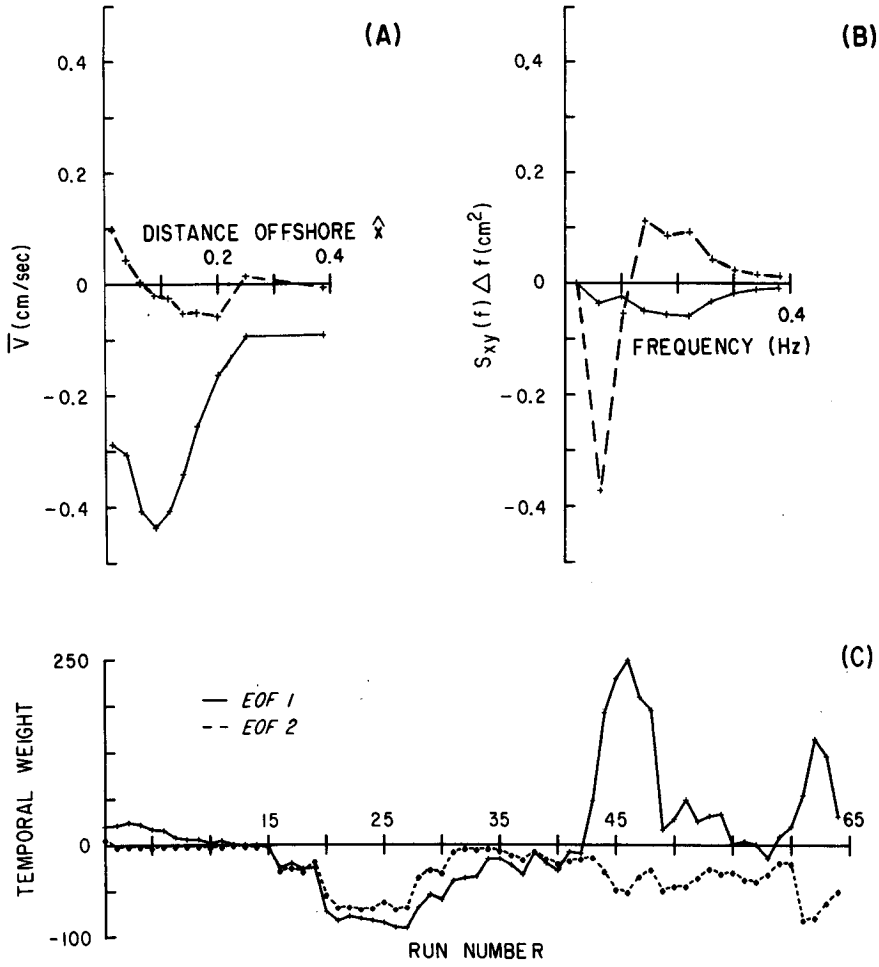

FIG. 13. Results of an EOF analysis using both longshore currents (ten spatial bins) and $S_{xy}(f)\Delta f$ (ten frequency bands). The weights (a) for currents and (b) for $S_{xy}(f)\Delta f$; solid line is first EOF, dashed line second EOF. (c) Temporal expansion coefficients (unitless) for EOF numbers 1 (solid line) and 2 (dashed line).

was stretched by the incident wave height. This stretching, however, did not increase the amount of current variance contained in the first EOF beyond that with a fixed cross-shore scale (93% in both cases). Similarly, in section 5 the temporal variation of the magnitude of the observed longshore current pattern was correlated with both the total applied stress [S^T_{xy}, Eq. (6)] and a dynamically based scale velocity [V^*, Eq. (11) after Longuet-Higgins, 1970]. For fixed S^T_{xy}, V^* decreases as the incident wave height increases because of the larger surf zone width and bed shear stress. The correlation was 0.97 in both cases. Thus, although much of the longshore current variability can be explained with conventional parameterizations (e.g., a variable surf zone width and V^*), the data do not conclusively support (or disprove) the utility of such parameterizations in a statistical sense. It is noteworthy that S^T_{xy} and E^T are themselves quite strongly correlated in this dataset (Fig. 5), which increases the difficulty of establishing the dependence of $\bar{V}$ on E^T. Additionally, many of the data runs with small $S^T{}_{xy}$ and $\bar{V}$ are of little quantitative value because errors in the mean flow measurements are comparable to the mean flow itself (e.g., runs 8, 56 and 58 in Fig. 9). Because these runs with weak flows are not much different from the mean state of nearly zero flow, the measurement errors do not substantially decrease the ability of the EOF representation to explain variation about the mean state. It is not possible, however, to use the noisy runs with small S^T_{xy} to examine the variation of the cross-shore structure of $\bar{V}$ with changes in E^T and approximately constant S^T_{xy}. At any rate, it is difficult to improve upon the large portion of the current variability explained with a constant cross-shore scale and regression with S^T_{xy}. A wider range of incident wave conditions (for example, constant and not small S^T_{xy} with a large variation in E) would probably provide a more enlightening test of Eq. (11) (or a more sophisticated scale

velocity, which is appropriate for arbitrary directional spectra). It is also possible that $\bar{V}$ has non-negligible vertical variation at the deeper stations, with flows maximum near the surface (such structure has been observed in rip currents). If this is the case, then the present velocity measurements, made near the seabed, would not fully reflect any increases in the cross-shore extent of the longshore current that occurred during large wave events.

Acknowledgments. Support for this analysis was received from NSF Grant OCE-8213657 (RTG and NC) and ONR Coastal Science Branch Contract NR388-114 (EBT). The Sea Grant Nearshore Sediment Transport Study (No. R/CA-N-4D) and ONR supported the data collection. R. J. Seymour obtained the bathymetric and slope array data. The staff of the Shore Processes Laboratory (Scripps Institution of Oceanography) installed and maintained the offshore sensors and data acquisition system. R. L. Lowe was the principal engineer. R. A. Dalrymple, J. Kirby and many others contributed substantially to the sensor maintenance. Their generous and untiring efforts are greatly appreciated.

REFERENCES

Allender, J. H., and J. D. Ditmars, 1981: Field measurements of longshore currents on a barred beach. *Coastal Eng.*, **5**, 295–309.

Aubrey, D. G., and J. H. Trowbridge, 1985: Kinematic and dynamic estimates from electromagnetic current meter data. *J. Geophys. Res.*, **90**(C5), 9137–9146.

Battjes, J. A., 1974: Computation of set-up, longshore currents, run-up and overtopping due to wind generated waves. *Communications on Hydraulics,* Delft University of Technology, Rep. 74-2, 244 pp.

Bowen, A. J., 1969: The generation of longshore currents on a plane beach. *J. Mar. Res.*, **27**, 206–215.

Cunningham, P. M., R. T. Guza and R. L. Lowe, 1979: Dynamic calibration of electromagnetic flow meters, *Proc. Oceans,* 1979, 298–301.

Derks, H., and M. J. F. Stive, 1984: Field investigations in the tow study programme for coastal sediment transport in the Netherlands. *Proc. 19th Conf. on Coastal Engineering,* Houston, ASCE, 1830–1845.

Gable, C. G., Ed., 1981: Report on data from the Nearshore Sediment Transport Study experiment on Leadbetter Beach, Santa Barbara, California, January–February 1980. IMR Ref. 80-5, Institute of Marine Resources, University of California.

Higgins, A. L., R. J. Seymour and S. S. Pawka, 1981: A compact representation of ocean wave directionality. *Appl. Ocean Res.*, **3**, 105–111.

Kraus, N. C., and T. O. Sasaki, 1979: Influence of wave angle and lateral mixing on the longshore current. *Mar. Sci. Commun.*, **5**(2), 91–126.

——, M. Isobe, H. Igarashi, T. O. Sasaki and K. Horikawa, 1982: Field experiments on longshore sand transport in the surf zone. *Proc. 18th Conf. on Coastal Engineering,* Cape Town, ASCE, 969–987.

Kundu, P. K., J. S. Allen and R. L. Smith, 1975: Modal decomposition of the velocity field near the Oregon Coast. *J. Phys. Oceanogr.*, **5**, 683–704.

Longuet-Higgins, M. S., 1970: Longshore currents generated by obliquely incident sea waves. *J. Geophys. Res.*, **75**, 6778–6801.

Oltman-Shay, J., and R. T. Guza, 1984: A data-adaptive ocean wave directional-spectrum estimator for pitch and roll type measurements. *J. Phys. Oceanogr.*, **14**, 1800–1810.

Putnam, J. A., W. H. Munk and M. A. Traylor, 1949: The prediction of longshore currents. *Trans. Amer. Geophys. Union.*, **30**, 337–345.

Thornton, E. B., 1970: Variation of longshore current across the surf zone. *Proc. 12th Conf. on Coastal Engineering,* Washington, DC, ASCE, 291–308.

——, and R. T. Guza, 1983: Transformation of wave height distribution. *J. Geophys. Res.*, **88**, 5925–5938.

——, and ——, 1986: Surf zone longshore currents and random waves: Field data and models. *Phys. Oceanogr.*, **16**, 1165–1178.

Van Heteren, J., and M. J. F. Stive, 1985: Kinematics and directionality of waves in the surf zone. Dept. Rijkswaterstaat of Ministry of Public Works, Rep. No. WWKZ-84. SO13, 52 pp. [Available from the Librarian, Delft Hydraulics Laboratory, P.O. Box 177, 2600 MH DELFT, The Netherlands.]

Wu, C.-S., E. B. Thornton and R. T. Guza, 1985: Waves and longshore currents: Comparison of a numerical model with field data, *J. Geophys. Res.*, **90**(C3), 4951–4958.